JM PAPERS

Direct detonation initiation in hydrogen/air mixture: effects of compositional gradient and hotspot condition

Xiongbin Jia[1,2], Yong Xu[2], Hongtao Zheng[1] and Huangwei Zhang[2],†

[1]College of Power and Energy Engineering, Harbin Engineering University, Harbin 150001, PR China

[2]Department of Mechanical Engineering, National University of Singapore, 9 Engineering Drive 1, Singapore 117576, Singapore

Two-dimensional simulations are conducted to investigate the direct initiation of cylindrical detonation in hydrogen/air mixtures with detailed chemistry. The effects of hotspot condition and mixture composition gradient on detonation initiation are studied. Different hotspot pressures and compositions are first considered in the uniform mixture. It is found that detonation initiation fails for low hotspot pressures and the critical regime dominates with high hotspot pressures. Detonation is directly initiated from the reactive hotspot, whilst it is ignited somewhere beyond the non-reactive hotspots. Two cell diverging patterns (i.e. abrupt and gradual) are identified and the detailed mechanisms are analysed. Moreover, cell coalescence occurs if many irregular cells are generated initially, which promotes the local cell growth. We also consider non-uniform detonable mixtures. The results show that the initiated detonation experiences self-sustaining propagation, highly unstable propagation and extinction in mixtures with a linearly decreasing equivalence ratio along the radial direction, i.e. $1 \rightarrow 0.9$, $1 \rightarrow 0.5$ and $1 \rightarrow 0$. Moreover, the hydrodynamic structure analysis shows that, for the self-sustaining detonations, the hydrodynamic thickness increases at the overdriven stage, decreases as the cells are generated and eventually becomes almost constant at the cell diverging stage, within which the sonic plane shows a 'sawtooth' pattern. However, in the detonation extinction cases, the hydrodynamic thickness continuously increases, and no 'sawtooth' sonic plane can be observed.

Key words: detonation waves, shock waves, combustion

1. Introduction

Detonation propulsion, e.g. a rotating detonation engine, has great potential because of its high thermal efficiency and simple structure (Wolanski 2013). Efficient detonation

† Email address for correspondence: Huangwei.zhang@nus.edu.sg

initiation is critical to materializing this technology with a compact engine structure and reliable operation. Typically, detonative combustion can be ignited by indirect and direct initiation. For the latter, a detonation can be initiated when the deposited energy is sufficiently high (Mazaheri 1997), e.g. through a spark gap (Matsui & Lee 1976) or detonating cord (Higgins, Radulescu & Lee 1998). However, due to extremely short space and time scales, detailed detonation initiation and development are difficult to capture experimentally (Radulescu *et al.* 2003), and hence our understanding about the underlying mechanism is still rather limited.

It is well known that a critical energy E_c exists to directly initiate a detonation wave in a detonable mixture (Zhang & Bai 2014). Depending on the deposited energy E_s, three regimes are identified: supercritical ($E_s > E_c$), critical ($E_s \approx E_c$) and subcritical ($E_s < E_c$) regimes (Ng & Lee 2003). Zeldovich (1956) proposed a theoretical model to determine the critical energy E_c, where E_c varies exponentially with the induction length. However, due to a series of simplifications involved, the criterion is applicable for stable detonation in which the induction length is relatively small. After that, several prediction models were developed, e.g. by Lee, Knystautas & Guirao (1982), Zhang, Ng & Lee (2012) and Ng (2005), in which an average delay in ignition is applied. The critical energy predicted by these models is in good agreement with the experimental data since well-estimated detonation parameters are incorporated, such as the detonation cell size and critical tube diameter. However, the detonation front is intrinsically unstable and exhibits a complex triple-point structure, which plays a key role in the direct detonation initiation (Shen & Parsani 2017).

Taking detonation curvature and unsteadiness into account, Kasimov & Stewart (2004) establish a prediction model as $\bar{D} - D - \kappa$ ($\bar{D}$ is detonation wave acceleration, D the detonation speed and κ the curvature), using single-step chemistry. Their model was improved by Soury & Mazaheri (2009), who incorporated detailed chemical kinetics and predicted better relations between E_c and the equivalence ratio. However, the model works for limited mixture composition due to the complex chemical reaction process and multi-dimensional effects during direct initiation (Zhang & Bai 2014). Furthermore, some details, including time-dependent detonation structure variations and the effects of unburned pockets on the direct initiation process, cannot be elucidated by these models.

Different from planar detonations, the curvature plays an important role in cylindrical and spherical detonations. He (1996), Eckett, Quirk & Shepherd (2000), Watt & Sharpe (2004, 2005) and Han *et al.* (2017) demonstrated the destabilizing effect of global curvature on detonation waves, and larger curvature would aggravate these effects. For instance, He (1996) found that a maximum curvature is defined by the nonlinear curvature effect, beyond which a self-sustaining detonation cannot be obtained. Eckett *et al.* (2000) pointed out that the unsteadiness in the induction zone is responsible for failure of detonation initiation. Watt & Sharpe (2004, 2005) showed that the pulsation amplitude arising from the curvature varies with the radius with which the detonation is first generated. Considering cellular stability, Han *et al.* (2017) found that the detonation structure evolves following three stages, i.e. no cell, growing cells and diverging cells. They also analysed the weakening effect of unburned pockets on the average detonation speed as the detonation cell increases (hence curvature decreases).

Parametric studies further our understanding of the direct initiation mechanism (Bradley *et al.* 2002; Qi & Chen 2017; Dai, Chen & Gan 2019; Gao, Dai & Chen 2020; Su, Dai & Chen 2021; Sun, Tian & Chen 2023). For instance, Bradley *et al.* (2002) propose a peninsula-shaped detonation regime in a two non-dimensional parameter $\xi - \varepsilon$ diagram for $H_2 + CO + \text{air}$ mixtures with various equivalence ratios. Differently, Gao *et al.* (2020)

find other regimes, i.e. C shape and rhino-horn shape for $H_2 +$ air mixtures by changing the initial pressure, temperature and equivalence ratio. Moreover, Chen and his coworkers conduct simulations focusing on multiple parameters, i.e. temperature perturbation (Qi & Chen 2017), CO_2 dilution (Dai *et al.* 2019), a kinetic model (Su *et al.* 2021) and ozone addition (Sun *et al.* 2023) and further demonstrate their respective effects on the detonation initiation regimes for extended mixtures.

Most previous work on direct initiation is focused on one-dimensional problems, where only longitudinal pulsating instability is incorporated (Eckett *et al.* 2000; Bradley *et al.* 2002; Ng & Lee 2003; Watt & Sharpe 2004; Watt & Sharpe 2005; Han *et al.* 2017; Qi & Chen 2017; Dai *et al.* 2019; Gao *et al.* 2020; Su *et al.* 2021; Sun *et al.* 2023). Nonetheless, in realistic situations, multi-dimensional cellular instability should be considered. Shen & Parsani (2017, 2019) study the effects of multi-dimensional instabilities on the direct initiation by comparing the phenomena from one- and two-dimensional simulations. Their results show that the one-dimensional configuration becomes invalid for unstable detonations. They also emphasize the important role of strong transverse waves from multi-dimensional instabilities in the failure and initiation processes of detonation. Moreover, Han, Kong & Law (2018) examine the effects of the activation energies of chemical kinetics on detonation initiation. They find that the continuous propagation of cellular detonation with higher activation energies exhibit a stronger dependence on regeneration of the transverse wave. Furthermore, Jiang *et al.* (2009) identify four mechanisms of the cell diverging in cylindrical detonation expansion based on two-dimensional simulations. This provides a deeper insight into the relation between flow instability and generating/diminishing transverse waves in different patterns. Besides, Asahara *et al.* (2012) further show the detailed Mach configuration and generation of sub-transverse waves during the cell diverging process.

Past work on direct detonation initiation is mostly concentrated on uniform mixtures. In practice, non-uniform mixtures widely exist in real-world applications, e.g. due to the insufficient mixing of fuel and oxidizer, which significantly affects the detonation initiation and development. Previous numerical works mainly focus on the detonation development in mixtures with gradient in tubes (Boeck, Berger & Sattelmayer 2016; Han, Wang & Law 2019; Lu, Kaplan & Oran 2023). Direct initiation in non-uniform mixtures in free space may be more complicated, including the curvature effects, which, to the best of our knowledge, is still lacking. Furthermore, the effects of hotspot properties (e.g. reactive, or non-reactive) on the mechanisms of detonation initiation have not been well understood. In the current study, we aim to examine the effects of hotspot properties and mixture composition gradient on direct detonation initiation. Two-dimensional simulations with a detailed chemical mechanism will be conducted. The manuscript is organized as follows: § 2 presents the governing equation and numerical method, whilst the results and discussion are detailed in §§ 3 and 4, respectively, followed by § 5 with conclusions.

2. Mathematical and physical models

2.1. *Numerical method*

The Navier–Stokes equations of mass, momentum, energy and species mass fractions are solved for compressible reacting flows, with the solver *RYrhoCentralFoam* (Zhao, Cleary & Zhang 2021). The accuracies of *RYrhoCentralFoam* in detonation simulations have been extensively validated (Huang *et al.* 2021), and it has been used for various detonation problems (Huang & Zhang 2020; Huang, Cleary & Zhang 2020; Xu, Zhao & Zhang 2021). The details on code validation for cylindrical detonation are given in the
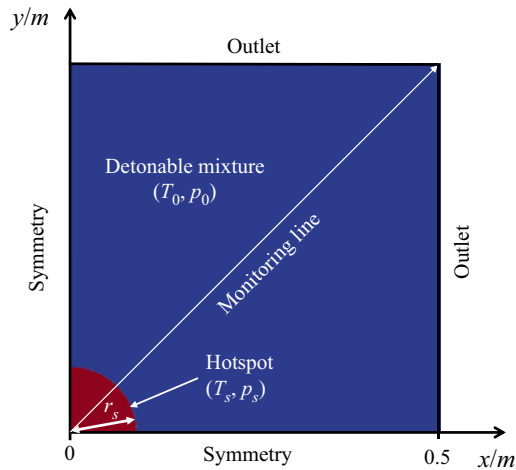
Figure 1. Schematic of the computational domain and boundary condition. Hotspot size not to scale.

supplementary material available at https://doi.org/10.1017/jfm.2023.512. A second-order implicit backward method is employed for temporal discretization, and the time step is 1×10^{-9} s. A Riemann-solver-free MUSCL (Monotone Upstream-centered Schemes for Conservation Laws) scheme (Kurganov, Noelle & Petrova 2001) with van Leer limiter is employed to calculate the convective fluxes in the momentum equations. The total variation diminishing scheme is used for the convection terms in the energy and species equations, whilst a second-order central differencing scheme is adopted for the diffusion terms in the equations of momentum, energy and species mass fractions (Greenshields *et al.* 2010; Huang *et al.* 2021). A detailed hydrogen mechanism is applied, with 13 species and 27 reactions (Burke *et al.* 2012). The chemical source term is integrated with an implicit Euler method.

2.2. *Physical problem and numerical implementation*

The expanding cylindrical detonation has the intrinsic characteristic of cellular instability, which plays an important role in initiation of transverse waves (Han *et al.* 2017; Shen & Parsani 2017). In this work, two-dimensional simulations (see figure 1) are conducted to capture the detonation frontal instability and dynamic behaviours. Due to the geometrical symmetry, a quarter area of the domain is simulated, and the domain is $0.5 \times 0.5 \, \text{m}^2$ (see figure 1). The *x* and *y* axes are aligned with the symmetry boundaries, and the radius is $R = \sqrt{(x^2 + y^2)}$. For two outlets, a wave-transmissive condition is enforced for the pressure, and a zero-gradient condition for all rest quantities.

The domain consists of two parts, as illustrated in figure 1. The first part is the circular hotspot with high temperature and pressure, (T_s, p_s), to mimic a localized ignition, e.g. resulting from additional energy deposition or shock focusing. The radius is fixed to be $r_s = 0.02 \, \text{m}$ in the simulations. The energy deposited in the hotspot is also clarified (Lee 1984), as listed in table 1. In this sense, the amount of energy deposited in the hotspot is large enough to create a significant thermochemical response leading to a strong blast wave in the reactive mixtures, resembling the classical instantaneous energy deposition to a point (Regele *et al.* 2016). Varying the hotspot size (Lee & Ramamurthi 1976; Mazaheri 1997) or thermodynamic perturbation addition near the hotspot (Qi & Chen 2017) may affect the detonation initiation (an effect of pressure perturbation near the hotspot is

970 A22-4

Case	Effects		Hotspot properties		Detonable mixture equivalence ratio	Regime
			Mixture	Energy		
A			$250P_0$; 2500 K; air	26 kJ		Critical
B		Pressure	$200P_0$; 2500 K; air	20.4 kJ		Critical
C	Hotspot properties		$150P_0$; 2500 K; air	15.6 kJ	1	Sub-critical
D			$100P_0$; 2500 K; air	10.4 kJ		Sub-critical
E		Composition	$100P_0$; 2500 K; $H_2 + $ air	26.8 kJ		Super-critical
F			$100P_0$; 2500 K; $H_2 + O_2$	29.2 kJ		Super-critical
G					$1 \rightarrow 0.9$	
H	Mixture composition gradients		$100P_0$; 2500 K; $H_2 + O_2$	29.2 kJ	$1 \rightarrow 0.5$	Super-critical
I					$1 \rightarrow 0$	

Table 1. Details of simulated cases.

shown in § D of the supplementary document), but we will not study it in this paper. Both non-reactive (the hotspot composition is air) and reactive ($H_2 + O_2$ or $H_2 + $ air) hotspots are considered.

The second part, beyond the hotspot, is filled with quiescent detonable gas, i.e. $H_2 + O_2 + N_2$ mixtures. The initial pressure is $p_0 = 20\ 265$ Pa and the initial temperature is $T_0 = 300$ K. Both uniform and varying composition of the detonable mixture will be studied. For the former, the composition of the gaseous mixture is H_2:O_2:$N_2 = 0.0282$:0.2255:0.7463 by mass. For the latter, a linear change of the equivalence ratio along the radial direction will be considered to examine its effects on detonation initiation and subsequent development.

Uniform 62.5 μm Cartesian cells are adopted to discretize the domain in figure 1, and the total mesh number is approximately 64 million. The half-reaction length from the theoretical Zel'dovich–von Neumann–Döring structure is approximately $l_{1/2} = 1$ mm, calculated by the shock and detonation toolbox (Shepherd 2021), and hence the foregoing mesh size corresponds to approximately 16 pts/$l_{1/2}$ for a Chapman–Jouguet (CJ) detonation. The mesh sensitivity test is shown in § A of the supplementary document, and the results show that mesh convergence can be obtained when the mesh resolution of 16 pts/$l_{1/2}$ is employed.

2.3. *Simulation case*

Parametric studies are performed and nine cases, i.e. A–I, are selected for discussion in this paper (see details in table 1). Specifically, case A–F have different hotspot parameters, whereas case F–I have different composition gradients in the detonable gas. When the air is filled in the hotspot, the critical regime dominates for relatively high p_0 (e.g. A and B), whereas the sub-critical regime dominates for low p_0 (e.g. C and D). Moreover, a super-critical regime is observed with reactive hotspots (e.g. E and F). To study the mixture composition gradients, a reactive hotspot with $H_2 + O_2$ (same as F) is selected to ensure successful initiation. Three equivalence ratio gradients are considered. Specifically, the equivalence ratio in the vicinity of the hotspot (the radius $R = 0.02$ m) is fixed to be 1, which decreases linearly to a certain value (e.g. 0.5, see table 1) at the outer edge ($R = 0.5$ m). For easy reference, we use an arrow to indicate the radial equivalence ratio (ER) change, e.g. $1 \rightarrow 0.9$ in case G.
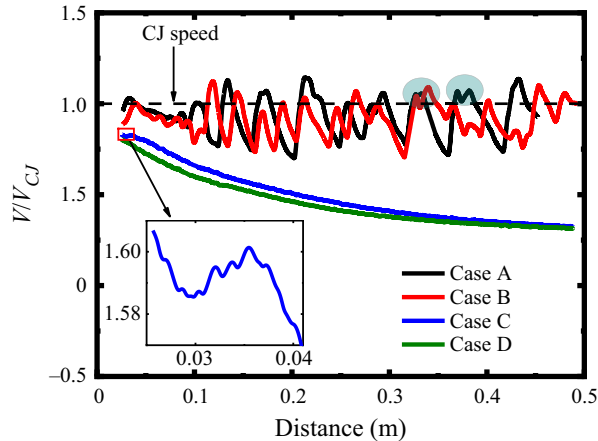
Figure 2. Change of the leading shock speed with radial distance when different hotspot pressures are considered (cases A−D).

3. Results

3.1. *Effects of hotspot properties*

In this section, we will study the effects of hotspot pressure and gas composition on the detonation initiation and development in a uniform detonable gas.

3.1.1. *Hotspot pressure effects*

Figure 2 shows the leading shock speed versus the radius with different hotspot pressures, i.e. $p_s = 250p_0$, $200p_0$, $150p_0$, $100p_0$. They are case A–D, and the hotspot is filled with air. The shock speed is estimated along the radial monitoring line (see figure 1). The detonation is successfully initiated only when $p_s \geq 200p_0$. Under relatively low hotspot pressures, the shock from the hotspot decelerates quickly and the detonation initiation fails. For instance, with $p_s = 150p_0$, the shock speed increases from 0.03 to 0.035 m after an initial drop (see the inset of figure 2). This is because intense reactions are triggered to release energy intensifying the shock. However, due to fast shock decay, the reaction front (RF) fails to coherently couple with the leading shock front (SF). Therefore, the latter degrades to a blast wave with a speed of around $0.3V_{CJ}$, corresponding to the sub-critical regime (Ng & Lee 2003).

With $p_s = 200p_0$ and $250p_0$, the shock from the ignition spot steepens into an overdriven detonation, due to the strengthening effects from the shocked mixture. The detonation gradually decays to a freely propagating detonation around 0.1 m. This can be categorized into the critical regime. The average propagation speed is slightly lower than the CJ speed, which is caused by the curvature effects (Ng & Lee 2003).

Figure 3 shows the detonation cell evolutions recorded from the peak pressure trajectories in cases A and B. For cylindrical detonations, the cell size λ is defined from the azimuthal direction (roughly perpendicular to the detonation propagation direction) (Lee 1984). For both cases, the detonation cell experiences three stages as the front curvature decreases: no cell (I), growing cells (II) and diverging cells (III), as annotated in figure 3. This is consistent with the observation by Han et al (2017). However, the detonation cell growth is not quantified in their study, and the detailed divergence process and mechanism still remain to be revealed. In the diverging cells stage, new cells are generated from the enlarged ones. Therefore, some small fluctuations of the shock speed along the monitoring
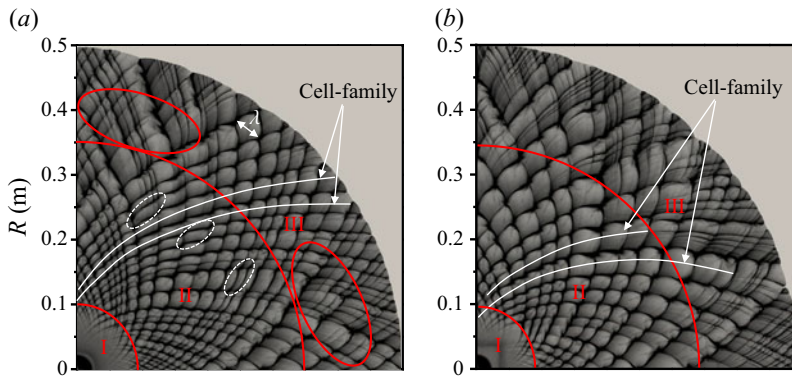
970 A22-6

Figure 3. Detonation cell evolutions with different hotspot pressures: (*a*) case A, $p_s = 250p_0$; (*b*) case B, $p_s = 200p_0$. Stage I: no cell; II: cell growing; III: cell diverging.

line are superimposed on the original periodic fluctuations, leading to double peaks, see the circles in figure 2. Besides, the detonation cell evolution before the cell divergence stage (III) is featured by a series of cell families. The results show that the number of detonation cells keeps almost constant as the cells grow. As such, the detonation cell increases linearly with the distance. Besides, higher hotspot pressure generates more cell families, corresponding to a globally smaller cell size. The calculated cell-family numbers in cases A and B are approximately 17 and 12, respectively. This is justifiable because a large hotspot pressure results in a high overdrive degree of the newly generated detonation wave. Besides, at $R > 3.5$ m, the cell begins to diverge in both cases. The divergence happens only in locally larger cells in case A (see red circles), but in a larger domain in case B with a greater growth rate.

3.1.2. *Hotspot composition effects*

Here, we will further examine the influences of hotspot composition on detonation initiation and development. Figure 4 shows the shock speed evolutions when two reactive hotspots are considered, i.e. stoichiometric $H_2 + $ air and $H_2 + O_2$ mixtures. They are cases E and F, respectively. The result with air hotspot (i.e. case D) is included for comparison. The hotspot pressure is $100p_0$. Different from the observation in § 3.1.1, an overdriven detonation is directly initiated and then decays to CJ detonation in both cases E and F, which corresponds to the super-critical regime (Ng & Lee 2003). As the overdrive degree decays, the periodic fluctuations of the shock speed occur earlier in case E, indicating an earlier onset of detonation cellularization. Furthermore, the speed fluctuation in case E exhibits more irregularity, especially at larger radii (hence smaller curvature).

Figure 5 shows the cell evolutions in cases E and F. In general, the cells in case F ($H_2 + O_2$) are smaller and more uniform. Only two stages appear, i.e. no cell (I) and growing cell (II). Even at the maximum radius in our simulation, the cell is still too small to diverge. Furthermore, in case E ($H_2 + $ air), some relatively small cells merge with the adjacent larger ones at the second stage, see the red circles in figure 5(*a*). This phenomenon will be further discussed in § 4.2. Moreover, cell divergence occurs at $R = 0.45$–0.5 m. The cell inhomogeneity and diverging behaviour lead to irregular shock speed fluctuations in figure 4. The cell-family number in E and F are 18 and 31, respectively. Consequently, the cell in F grows more slowly and its maximum cell size reaches approximately 27 mm, slightly smaller than the theoretical value, 28.9 mm (Ng, Ju & Lee 2007). In this sense,
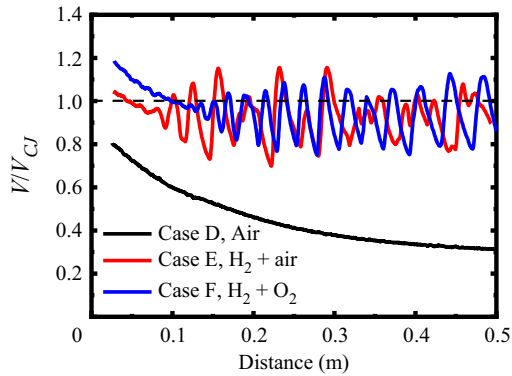
Figure 4. Change of the leading shock speed with radial distance in cases D−F. $p_s = 100p_0$. Dotted horizontal line: CJ speed.
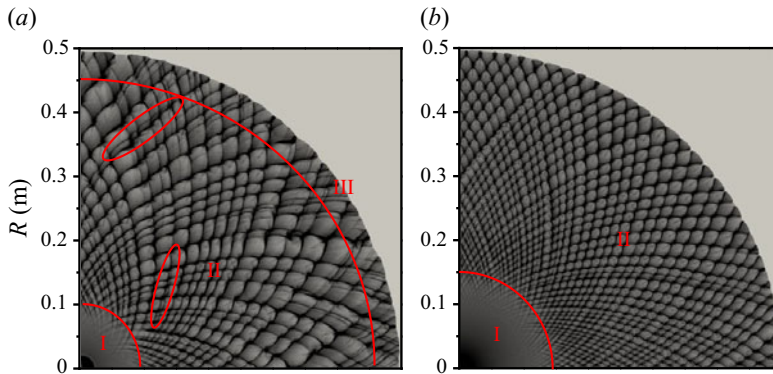

Figure 5. Detonation cell evolutions with different hotspot compositions: (*a*) case E: stoichiometric $H_2 + air$ mixture; (*b*) case F: stoichiometric $H_2 + O_2$ mixture. Stage I: no cell; II: cell growing; III: cell diverging.

the detonation can still propagate in a self-sustaining fashion without new cell generation. Combined with figure 3, it can be found that there exists a range within which cell divergence is more likely to take place, and in § 4.2 we will further study this range.

3.2. *Effects of composition gradient in the detonable mixture*

In this section, we will study detonation initiation in $H_2 + air$ mixtures with a spatially varying equivalence ratio. Specifically, the ER in the vicinity of the hotspot is 1, and then decreases linearly to 0.9, 0.5 and 0 at $R = 0.5$ m in cases G, H and I, respectively. A hotspot ($100p_0$, 2500 K) with a stoichiometric $H_2 + O_2$ mixture is employed, the same as that in case F.

Figure 6 shows the variations of the leading shock speed in cases F–H along the monitoring line. Since the reactive hotspot ($H_2 + O_2$) is employed, overdriven detonations are directly triggered by it in all cases. Generally, their shock speeds are close before 0.1 m, due to the near-stoichiometric ERs. Beyond that, significant differences appear when the multi-headed detonations start to develop, featured by various speed fluctuations. Among them, continuous detonation propagation happens only in cases F (uniform, $\varphi: 1 \rightarrow 1$) and G ($\varphi: 1 \rightarrow 0.9$). The average shock speed during the cellular detonation stage ($R = 0.12$–0.5 m) in G is 1756 m s^{-1}, slightly lower than that in F (1768 m s^{-1}) since the mixture
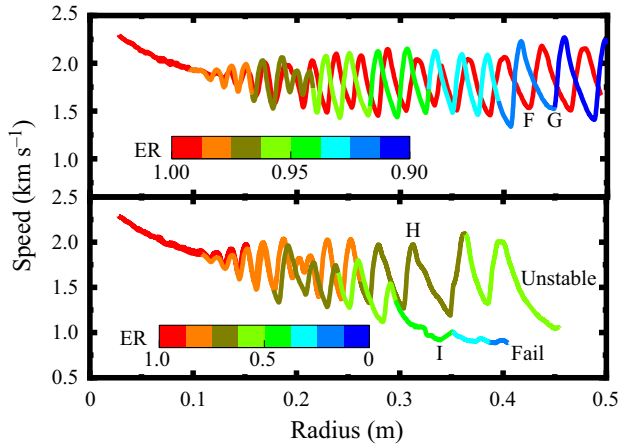
970 A22-8

Figure 6. Change of the leading shock speed with radial distance in cases F−I. The profiles are coloured by the local equivalence ratio.
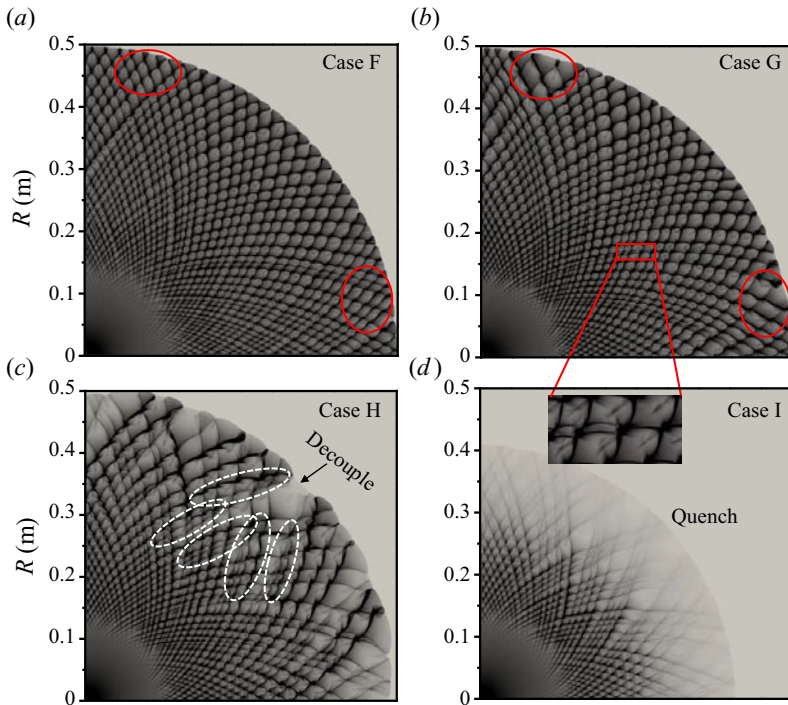

Figure 7. Detonation cell evolution with different mixture composition gradients in cases F–I.

reactivity decreases slightly in the former case (see § C of the supplementary document). Moreover, in cases H and I, the overdriven detonation gradually decouples when it runs outwardly. Specifically, in case H ($\varphi: 1 \to 0.5$), when the shock propagates across $R = 0.3$ m (the local ER is $\varphi = 0.71$), the period of speed fluctuation increases significantly, indicating a more unstable detonation front. In case I ($\varphi: 1 \to 0$), the detonation wave quickly decouples across $R = 0.3$ m ($\varphi = 0.42$) with a shock speed below 900 m s^{-1}.

Figure 7 shows the detonation cell evolutions in cases F–I. Almost uniform cells appear at approximately 0.15 m and grow until 0.5 m in both F and G, except for locally larger
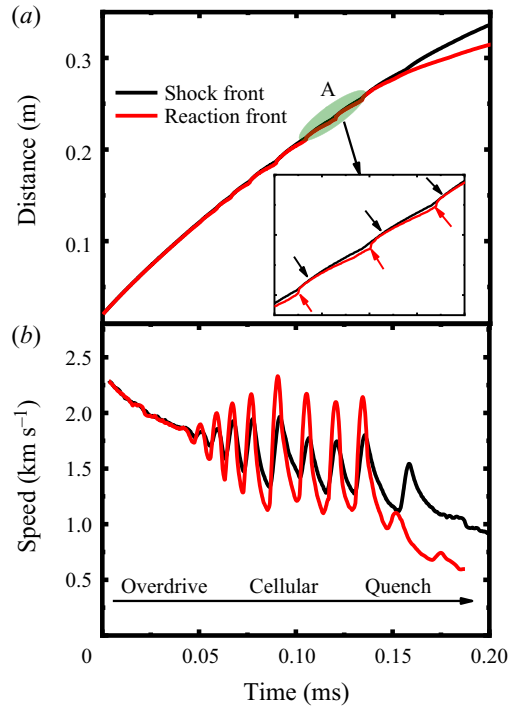
Figure 8. Time history of (*a*) SF and RF position and (*b*) propagation speed along the monitoring line in case I.

cells, as annotated by the red circles in figures 7(*a*) and 7(*b*). This phenomenon is attributed to the cell-family differences (i.e. 31 for F, 27 for G) and cell coalescence (see the inset in figure 7), which are caused by the drop of mixture reactivity with the decrease of ER in case G, especially at larger radii (see § C of the supplementary document).

Increased composition gradient in cases H and I leads to a remarkable change of the detonation cell distribution, as shown in figures 7(*c*) and 7(*d*). In case H ($\varphi: 1 \to 0.5$), the cells grow steadily from $R = 0.15$ to 0.3 m and remain diamond shaped. Beyond that, they become irregular, and some cells grow faster and then merge with the adjacent smaller cells. As the detonation propagates across $R = 0.25$ m ($\varphi = 0.75$), irregular cells grow as the reactivity of mixtures drops significantly (see § C of the supplementary document). Therefore, apart from the curvature decrease, which leads to the increase of the detonation cell size, the cell coalescence induced by the ER variation plays a more important role in the oversized cell generation. This oversized cell further causes the local detonation quenching. At around $R = 0.5$ m ($\varphi = 0.5$), the detonation becomes very unstable and detonative combustion is even quenched at most of the front. In case I ($\varphi: 1 \to 0$), the detonation cells appear at around $R = 0.13$ m and grow slightly until 0.3 m, like the rest of the cases in figure 7. However, detonation extinction happens beyond $R = 0.3$ m ($\varphi = 0.42$) due to a dramatic drop of mixture reactivity (see § C of the supplementary document), with quickly faded peak pressure trajectories in figure 7(*d*).

Figure 8 shows the time evolutions of the shock speed and SF/RF position along the monitoring line in case I. Three stages can be identified: overdriven detonation (0–0.05 ms), cellular detonation (0.5–0.13 ms) and detonation quenching (0.13–0.2 ms). At the cellular detonation stage, the shock speed experiences periodic variations with
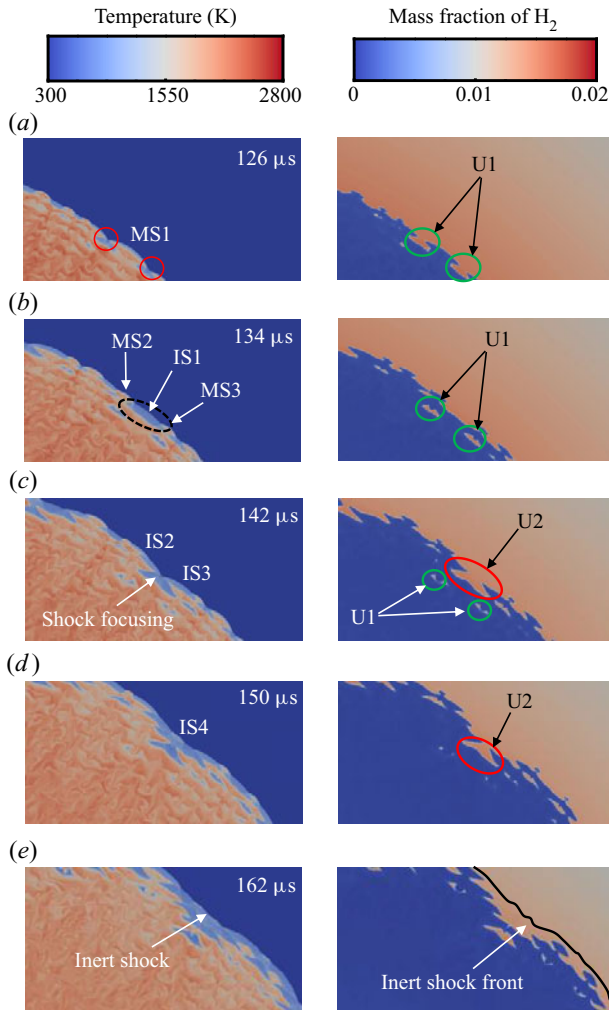
970 A22-10

Figure 9. Time sequence of temperature and hydrogen mass fraction in case I.

an increasing time interval. The inset in figure 8(*a*) provides the change of SF/RF in the cellular detonation stage. The red arrows indicate the abrupt acceleration of the RF, whereas the black ones point to the generation of the Mach stem (MS). From figure 8(*b*), the speeds of both fronts fluctuate after 0.05 ms and the periodic variations of the SF speed are delayed relative to that of the RF, manifesting an intrinsic characteristic of unstable cellular detonation. From 0.13 ms, the RF speed continuously decreases and is lower than that of the SF, which indicates the decoupling of SF and RF.

Figure 9 shows the distributions of temperature and hydrogen mass fraction at different instants during the detonation extinction process in case I. From 126–134 μs, the Mach stem, MS1, gradually attenuates and evolves to an incident shock, IS1, with the unburned pocket 1 (U1) left behind, which weakens the SF intensity. Meanwhile, a longer induction zone is formed behind IS1. Two detonation bubbles are generated from the local explosion induced by shock focusing (Lee 2008) (see the red circle at 126 μs), which evolves into the MS2 and MS3 (see 134 μs). Due to the increased induction length, the new ISs collide with each other, leading to weaker focusing energy (see 142 μs). Therefore, another larger
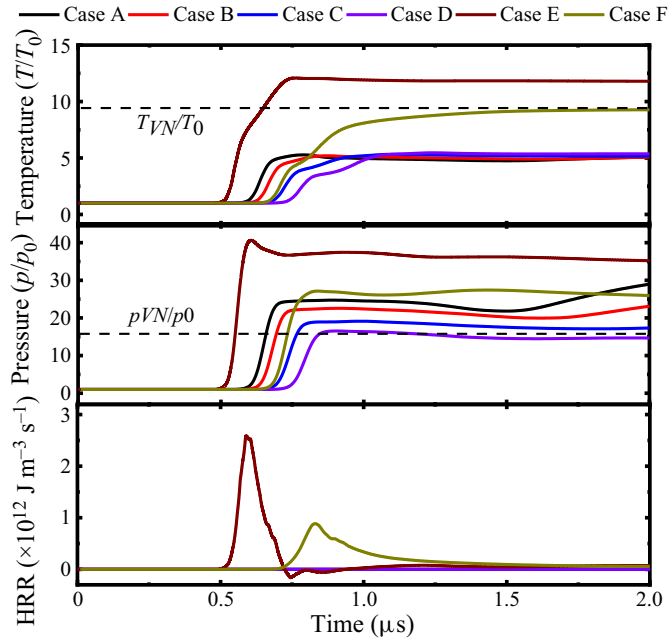
970 A22-11

Figure 10. Evolutions of (*a*) temperature, (*b*) pressure and (*c*) HRR from the probe ($R = 21$ mm). The von Neumann states are from the detonable gas condition ($H_2 + $ air mixture).

unburned pocket (U2) is generated, which further reduces the local heat release. Another new IS4 develops from the focusing and propagates outwardly; however, the reaction cannot be triggered by this weak focusing, e.g. at 150 μs. Consequently, the detonation quenches and further degenerates into an inert shock wave at 162 μs. Meanwhile, when the RF and SF are fully decoupled (at 162 μs), considerable unburned H_2 exists behind the shock, and the low temperature can be found between the SF and RF.

4. Discussion

4.1. *Hotspot evolution and its relevance to detonation initiation*

Hotspot evolution and its relevance to detonation initiation will be discussed here based on cases A–F. Figure 10 shows the time history of temperature, pressure and heat release rate (HRR), from a probe of $R = 21$ mm, i.e. 1 mm off the hotspot vicinity along the monitoring line. It is shown that intense chemical reactions take place in two reactive hotspots (i.e. cases E and F) with the maximum pressure and temperature higher than the corresponding von Neumann values. This indicates that the detonations are initiated directly from the hotspot. Note that the detonation in case E manifests a higher overdrive degree ($f = 1.41$) than that in F ($f = 1.09$) due to higher oxygen concentration (Short & Stewart 1999). As the overdriven detonation expands outwardly, the probe (i.e. already in the post-detonation area) temperature and pressure decrease gradually towards a constant value, whereas the HRR is reduced to almost zero.

Figure 11(*a*) shows the evolutions of the reactive hotspot along the monitoring line from 10 to 110 ns in case F ($H_2 + O_2$ hotspot, $p_s = 150p_0$). The reader should be reminded that, due to one-dimensional nature of early shock/detonation structures, the results in figure 11 do not exhibit azimuthal variations. Homogeneous isochoric reactions occur
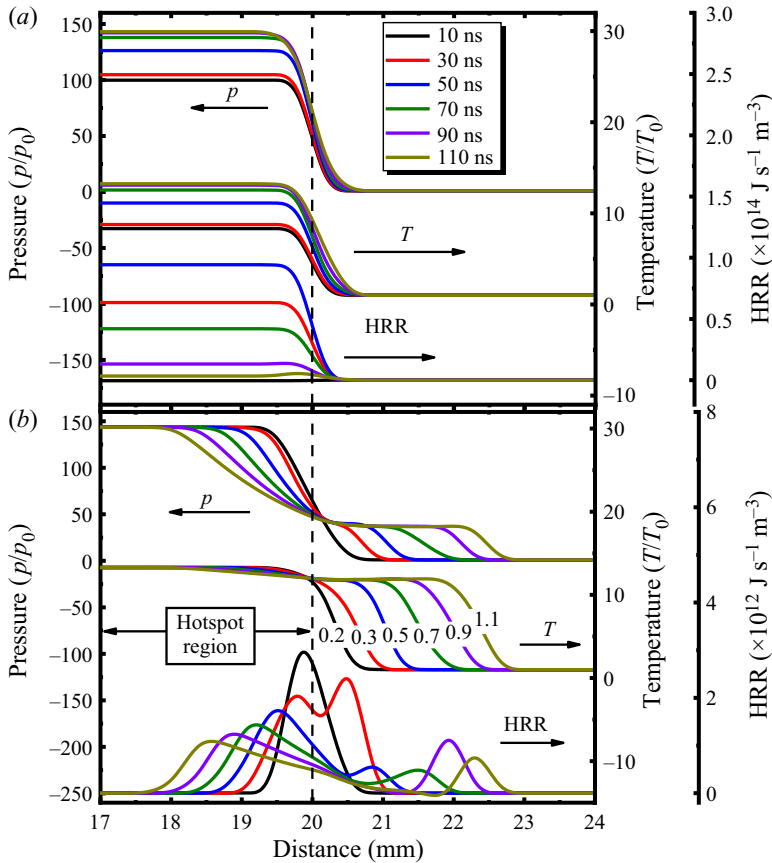
970 A22-12

Figure 11. Changes of pressure, temperature and HRR in the hotspot at (*a*) 10–110 ns and (*b*) 0.2–1.1 μs in case F. Time stamps in (*b*) are in microseconds.

inside the spot, leading to quickly increased pressure and temperature. The HRR peaks at approximately 41.5 ns, and then quickly decreases to low values at around 110 ns. Meanwhile, the hotspot pressure and temperature remain unchanged from 90 to 110 ns, indicating the completion of chemical reactions in the hotspot. During this period, the premixture outside the hotspot remains intact; see figure 11(*a*). The hotspot reaction leads to increased pressure and temperature gradients at the hotspot vicinity, which play an important role in initiating a detonation (Gu, Emerson & Bradley 2003).

Plotted in figure 11(*b*) are the state evolutions at the hotspot vicinity after 0.2 μs. Apparently, an outwardly propagating SF (the shock pressure is around $40p_0$) emanating from the hotspot vicinity can be observed. It arrives at the probe at around 0.5 μs, resulting in a pronounced pressure rise, as shown in figure 10. An RF trails behind the shock, burning the compressed $H_2 + air$ mixture, featured by high HRR. Their mutual reinforcement quickly initiates a developing detonation, as found from the subsequent instants (0.7–1.1 μs) in figure 11(*b*). Furthermore, the corresponding evolutions of λ_{CEM}, a chemically explosive mode (Lu *et al.* 2010; Goussis *et al.* 2021), along the monitoring line are shown in figure 14(*a*). Note that the chemical explosive mode (CEM) is a chemical property of local gaseous mixture and characterizes the chemical explosion propensity of the shocked gas, and hence has been extensively employed in transient detonation
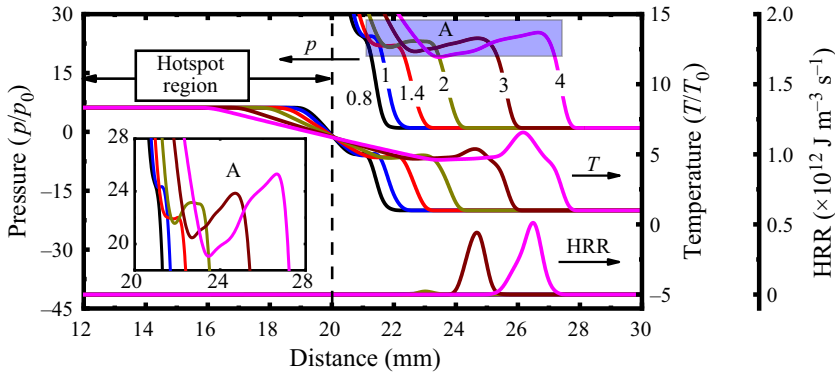
970 A22-13

Figure 12. Changes of pressure, temperature and HRR near the hotspot at 0.8–2 μs in case A. Time stamps in microseconds.

problems (Xu *et al.* 2021; Guo *et al.* 2022; Jin *et al.* 2023). The value of λ_{CEM} corresponds to the reciprocal time scale of the chemical explosion. Finite λ_{CEM} exists near the hotspot vicinity, as shown in figure 14(*a*), manifesting the locally strong reactivity, which induces the immediate onset of detonation. Besides, there is a secondary inwardly propagating RF in the spot in figure 11(*b*). This may be attributed to chemical reactions as the local temperature drops due to thermal diffusion (see figure 11*b*). In addition, the hotspot evolution in case E is generally like that in F, but the shock arrives at the probe around 0.2 μs later, due to a slower speed.

Differently, for non-reactive hotspots in cases A–D, we can see from figure 10 that, although the maximum pressure exceeds the von Neumann values, their maximum temperatures are much lower than the respective von Neumann values. Furthermore, their peak HRRs that occur downstream of the hotspot are almost four orders of magnitude smaller than those in E and F. All these indicate that only shock compression occurs there and detonation has not developed yet. As shown in § 3, detonations are ultimately initiated in cases A and B. Therefore, it is interesting to further investigate how they are generated with a shock from the hotspot.

We first look at case A, and the corresponding hotspot evolutions along the monitoring line from 0.8 to 2 μs are shown in figure 12. Note that the pressure inside the spot is maintained at the initial value, i.e. $250p_0$, since no reactions happen therein (not displayed in figure 12). At larger radii, e.g. at $R = 21$–28 mm, the pressure peak first deceases and then increases, see the inset of figure 12. This is because the leading shock, generated at the hotspot vicinity, decays as it travels outwardly (see the HRR profiles, 0.8–1.4 μs). The peak pressure at 1.4 μs is around $22p_0$, 1.4 times the von Neumann value, whilst the peak HRR reaches around 1.5×10^9 J m^{-3} s^{-1} (not shown in figure 12). Subsequently, the reactions start in the shocked mixture (2–3 mm off the hotspot) at approximately 2 μs, and the peak HRR increases to around 5×10^{11} J m^{-3} s^{-1} at 3–4 μs. This indicates the formation of a shock-induced auto-igniting RF and its acceleration behind the leading SF (Gu *et al.* 2003). As the RF couples to the leading SF, the detonation is initiated. In this case, λ_{CEM} keeps zero close to the hotspot (see figure 14*b*), increases immediately behind the SF and peaks at the RF from 1 to 2 μs. As the autoignition wave approaches the SF, the distribution of λ_{CEM} shows double peaks at 3–4 μs and the λ_{CEM} rises dramatically behind the SF. This detonation initiation fashion differs from those in cases E and F, where the unburned mixture is directly ignited by the detonation from the hotspot. As such, it can be expected that detonation initiation beyond the hotspot is more affected by reactivity of
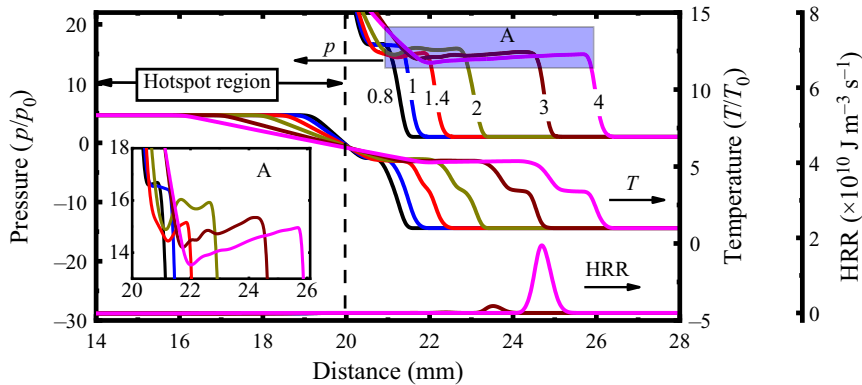
970 A22-14

Figure 13. Changes of pressure, temperature and HRR in the hotspot at 0.8–4 μs in case D. Time stamps in microseconds.

the detonable mixture, besides the hotspot itself. The hotspot evolution in case B is like that in A, but with a delayed detonation initiation. The shock wave arrives at the probe 0.02 μs later than that in case A, see figure 10.

Figure 13 shows the hotspot evolution along the monitoring line in case D. Similar to case A, the pressure peak drops initially (0.8–1.4 μs) and then increase (2 μs). However, it drops again from 2 to 4 μs; see the inset in figure 13. This is because, although the reaction contributes to the shock amplification, the peak pressure remains only 14–$16p_0$, close to the von Neumann value ($15.1p_0$) (Shepherd 2021). Furthermore, the thermally neutral zone is continuously lengthened from 2 to 4 μs. The auto-ignition RF is also ignited like case A. Nonetheless, the RF cannot synchronize with the leading SF, eventually failing to initiate the detonation. Different from case A, the distribution of CEM shows one single peak at 3–4 μs in case D (see figure 14c), and an obvious plateau appears during the rise of the λ_{CEM} (see A region in figure 14c) at 4 μs due to the decoupling of the RF and SF. Actually, during the later propagation of the shock, no detonation development (e.g. deflagration-to-detonation transition) is found. In another detonation failure case, C, hotspot evolution is generally similar to that in case D.

To generalize the hotspot effects, we conduct a series of simulations by changing the hotspot pressure for both non-reactive (i.e. air) and reactive (i.e. $H_2 + O_2$ and $H_2 +$ air) hotspots. Figure 15 shows the probe pressure (p_p) and temperature (T_p) as functions of the hotspot pressure (p_s) at the probe ($R = 21$ mm). Since the isochoric reactions first take place inside the spot for reactive hotspots (i.e. $H_2 + O_2$, $H_2 +$ air), we also present the maximum pressure (p_{max}/p_0) and temperature (T_{max}/T_0) when the reactions are completed in the hotspot.

Generally, detonations are not initiated directly from all non-reactive hotspots regardless of their pressure; see the probe temperature in figure 15(a). When the hotspot pressure is $p_s = 50$–$300p_0$, the detonation can be initiated somewhere beyond the hotspot only when $p_s \geq 200p_0$. Moreover, detonation initiation depends on whether the shock is strong enough to ignite the detonable mixture followed. For the studied cases, the peak probe pressure should be at least 1.5 times the von Neumann pressure for successful initiation. It is seen from figure 15(a) that the probe pressure p_p increases monotonically with p_s, but with a decreasing slope, whilst the probe temperature T_p increases almost linearly with p_s. The detonation cannot be initiated beyond the hotspot when p_s decreases to $\leq 150p_0$. Although the probe pressure for $p_s = 100p_0$ or $150p_0$ slightly exceeds the von Neumann spike, the
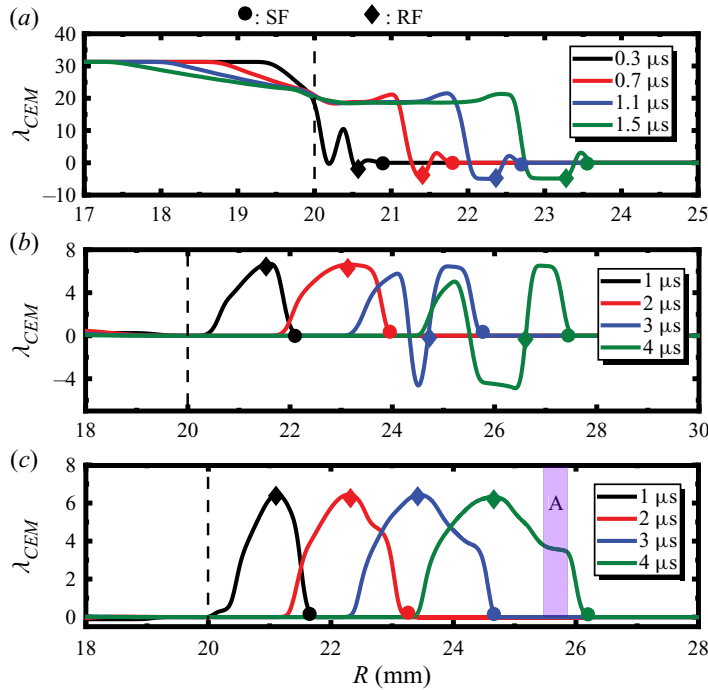
Figure 14. Evolutions of the chemical explosion mode along the monitoring line during the hotspot development. (*a*) Case F, (*b*) case A, (*c*) case D. Dotted vertical lines: hotspot vicinity.

RF is too weak and eventually the detonation initiation is not successful (marked as 'Fail' in figure 15*a*).

For the reactive hotspot cases in figure 15(*b*), the detonation can be directly initiated due to the significant gradient of thermochemical states at the spot vicinity under appropriate p_s (i.e. $p_s \geq 50p_0$ for $H_2 + O_2$ hotspot and $p_s \geq 100p_0$ for $H_2 +$ air hotspot). No detonations can be initiated when the hotspot pressure decreases to $10p_0$ for the $H_2 + O_2$ hotspots and $\leq 50p_0$ for the $H_2 +$ air hotspots (annotated with 'Fail' in figure 15*b*). Based on the current simulations, detonation initiation by the shock beyond the reactive hotspot is not observed.

As the hotspot pressure increases, the peak hotspot pressure p_{max} due to the isochoric reactions increases linearly (see figure 15*b*). However, the peak hotspot temperature increases dramatically when $p_s \leq 150p_0$; beyond that, it grows slowly when the hotspot pressure further increases. This is because the chemical equilibrium moves towards the exothermic reaction direction and gradually approaches the limit. Furthermore, both probe pressure p_p and temperature T_p monotonically increase with the initial pressure of the reactive hotspots, and the growth rate decreases with the hotspot pressure. This is similar to what is seen from the non-reactive hotspots in figure 15(*a*).

4.2. *Detonation cell diverging and coalescence*

As the cellular instability increases to a certain threshold value as the detonation propagates outwardly, additional transverse waves would be generated to match the growing surface of the detonation for self-sustaining propagation (Jiang *et al.* 2009; Han *et al.* 2017). In this section, we will discuss two patterns of cell divergence observed from case B (see figure 3*b*): abrupt and gradual divergence, respectively, in figures 16(*a*) and
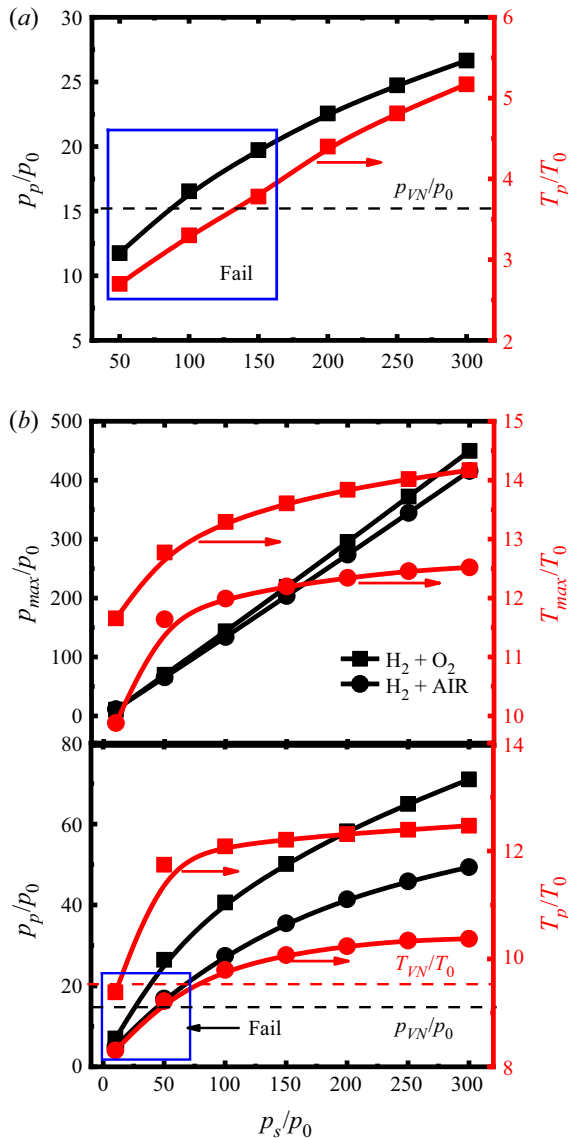
970 A22-16

Figure 15. Change of pressure and temperature at the probe ($R = 21$ mm) with different hotspot pressures: (*a*) non-reactive hotspot and (*b*) reactive hotspot.

16(*b*). In the abrupt pattern, as the cell C1 grows and develops into C2 after the next triple point is generated, the secondary peak pressure is elevated in C2, signifying the formation of new cells in it. Nonetheless, for the gradual pattern, relatively weak pressure waves are generated in C4. With the shock interaction between C4 and C5, the forgoing weak pressure becomes stronger in C5, and eventually new secondary cells are generated in C5. The growth rate of cell size from C1 to C2 is 50 %, much higher than that (9 %) from C3 to C4. This difference is responsible for various cell diverging patterns and the details will be presented in figures 17 and 18.

Figure 17 shows the pressure gradient magnitude and temperature distributions during the abruptly diverging transient. The MS from the triple point is smooth initially (e.g.
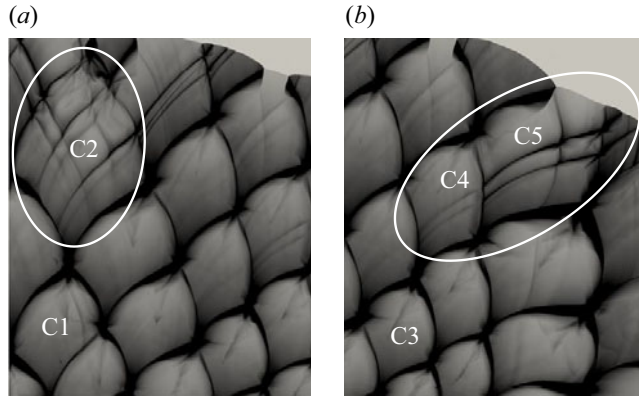
Figure 16. Detonation cell diverging in case B: (*a*) abrupt pattern and (*b*) gradual pattern.
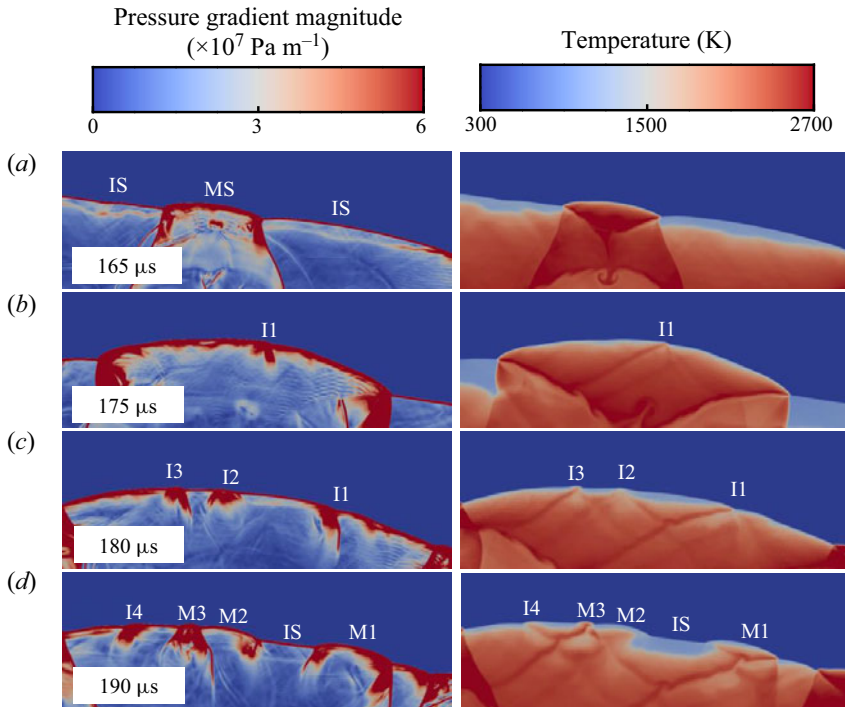

Figure 17. Evolution of abrupt cell divergence: pressure gradient magnitude (left column) and temperature (right column).

at 165 µs). Its velocity is higher than the adjacent ISs. As the curved MS propagates outwardly, its surface significantly increases, leading to decreasing number of cells per unit area of the detonation front. Consequently, instability 1 (I1 in figure 17*b*) occurs along the MS, leading to front wrinkling (Shen & Parsani 2017). Moreover, the temperature near I1 is higher than that of the surrounding (see 175 µs), corresponding to higher local reactivity. The shock near I1 propagates with a greater speed, causing a convex front. The transverse wave originating from I1 propagates circumferentially and interacts with IS, further intensifying I1, see 180 µs. Other instabilities, e.g. I2 and I3, appear due to

Pressure gradient magnitude
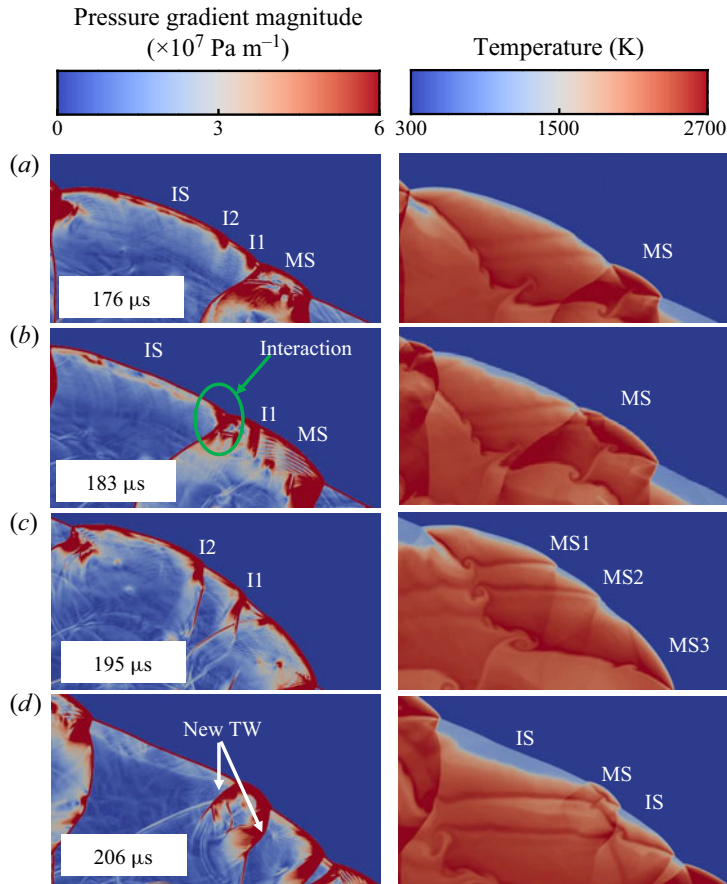$(\times 10^7 \ \mathrm{Pa \ m^{-1}})$

Temperature (K)

Figure 18. Evolution of gradual cell divergence: pressure gradient magnitude (left column) and temperature (right column).

the similar mechanism. As the MS decays, a thin gap is generated between the leading SF and RF, and the temperature therein is lower (see 180 μs), indicating the increased induction time. The mixtures near the instabilities are more explosive, eventually resulting in an RF. The RF then couples to the SF, and new MSs are developed, e.g. at 190 μs; MS1-3 originates from I1-3, respectively. Meanwhile, new instability I4 is generated due to increased detonation surface. The detonation front is divided into several sections, with staggered MS and IS.

Evolution of the gradually diverging pattern is detailed in figure 18. The occurrence of instabilities is like those in the abrupt pattern, but they are too weak to induce new cells when the detonation expands. Instead, the instability amplification during the interactions between two adjacent shocks plays an important role in the divergence process. In figure 18, the instabilities I1 and I2 only occur along the IS at 176 μs. As the adjacent MS expands, it collides with the neighbouring shock; I1 is obviously intensified after collision with the transverse wave of the MS; see 183 μs. This also induces the wrinkled MS. Besides, the interaction between two opposite transverse waves originating from I2 and MS, respectively, can be observed, as marked by the green circle in figure 18(*b*). After the instability amplification from IS to the adjacent MS, the subsequent diverging behaviour is like that from the abrupt pattern. At 195 μs, new hotspots evolve from the instability,
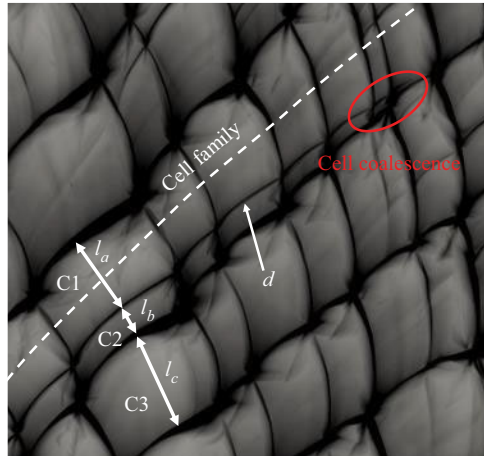
Figure 19. Distributions of the peak pressure trajectories in a cell coalescence process in figure 5(*a*).

generating new MSs. Finally, new cellular features, including MS, IS and transverse wave (TW), appear at 206 µs.

Another phenomenon worthy of discussion at the cell-growth stage is cell coalescence. In contrast to the diverging behaviours, the cell coalescence always takes place where the initial irregular cell pattern dominates, which subsequently generates larger local cells. Figure 19 shows a detailed coalescence process in case E, as demonstrated in figure 5(*a*). To better illustrate the underpinning mechanism, a relative cell size (i.e. cell thickness in this work) perpendicular to the cell-family direction is introduced, denoted by l_a–l_c in figure 19. The cell thickness of C2 is only around a third of C1 or C3, giving a high instability as the detonation propagates outwardly. Furthermore, as C1 and C3 grow along the cell family, C2 further decreases until ultimate disappearance.

Figure 20 shows the cell coalescence transient, using the pressure gradient magnitude and temperature distributions at successive instants. At 53 µs, MS1 is generated with intense chemical reactions accompanied by two strong transverse waves, T2 and T3. Meanwhile, a relatively weak transverse wave T1 propagates towards T2. After the collision between T1 and T2, MS2 is generated near MS1, and its speed is larger than that of MS1. As such, two adjacent MSs (MS1 and MS2) form a large MS along with three TWs, among which T1 and T3 propagate in the same direction. The trajectory of T1 can be found in figure 19 (see *d*). As the detonation evolves, T1 gradually approaches T3. As T1 coalesces with T3 and further collides with T4 (see 59–61 µs, figure 20), a new hotspot is generated with local high reactivity (see the circled region, 61 µs), accompanied by the disappearance of T3.

To quantify the cell variations as the detonation wave propagates outwardly, in figure 21 we show the calculated cell size from uniform and non-uniform detonable mixtures. Here, the cell size is approximated by the radial distance between A and B along the arc R_1, as shown in figure 21(*a*). The fitted line is plotted by the proportional relation between a certain arc and the number of cell families, as shown in figures 21(*b*) and 21(*c*). The cell-family number remains constant before diverging in cases A, B and F (see figures 3 and 5*b*), and decreases due to cell coalescence for cases E and G−I. (see figures 5*a* and 7). Consequently, the fitted lines feature constant, for cases A, B, F, and increasing slopes for cases E and G−I, see figures 21(*b*) and 21(*c*). Note that they are obtained from
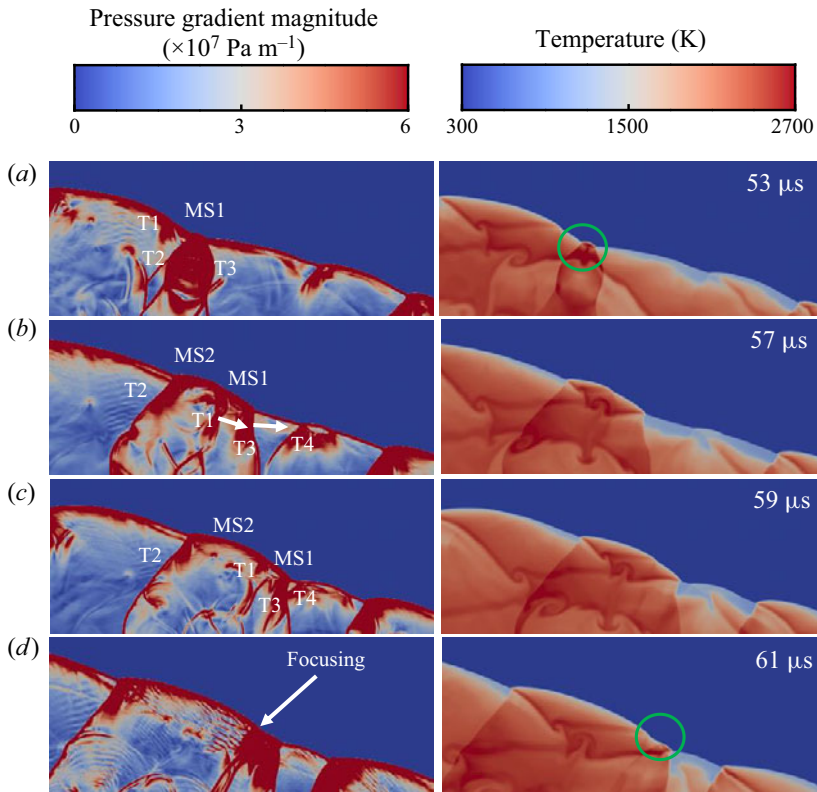
Figure 20. Evolution of the cell coalescence in figure 19: pressure gradient magnitude (left column) and temperature (right column).

the cell-growth stage in all cases. The theoretical cell size with the Ng correlation (Ng *et al.* 2007) and the experimental data by Stamps & Tieszen (1991) are also presented for reference in the uniform case.

Generally, the cell-growth rate decreases (hence cell-family number increases) with hotspot pressure for non-reactive hotspots A and B. This can be ascribed to higher detonation strength in case A as the cellular detonation initially forms. Besides, a lower cell-growth rate of case F can be found from figure 21(*b*) due to higher overdrive. For cases A, B and E, the detonation cell starts to diverge when the cell size approaches a certain value. It can be inferred from figure 21(*b*) that this threshold is a value greater than the corresponding theoretical and experimental cell sizes, under which condition the detonation propagates at a relatively stable state (Lee 1984). When the cylindrical detonation expands, the collisions between adjacent transverse waves become difficult due to increased spacing. Accordingly, the cellular instability significantly increases, especially as the average cell size continuously grows beyond the characteristic cell size. This enhanced instability leads to generation of new transverse waves to sustain detonation propagation (Jiang *et al.* 2009). In the studied cases, the threshold value is 1.4–2 times the characteristic cell size under the same mixture condition. It is worth noting that a real three-dimensional detonation structure is very complex, involving irregularity and inhomogeneity of the detonation cell (Pintgen *et al.* 2003; Crane *et al.* 2023), which may lead to greater fluctuations of the threshold than that in the current simulations. For case F, the sizes of cell samples at various radii are closer to the fitted line due to the more
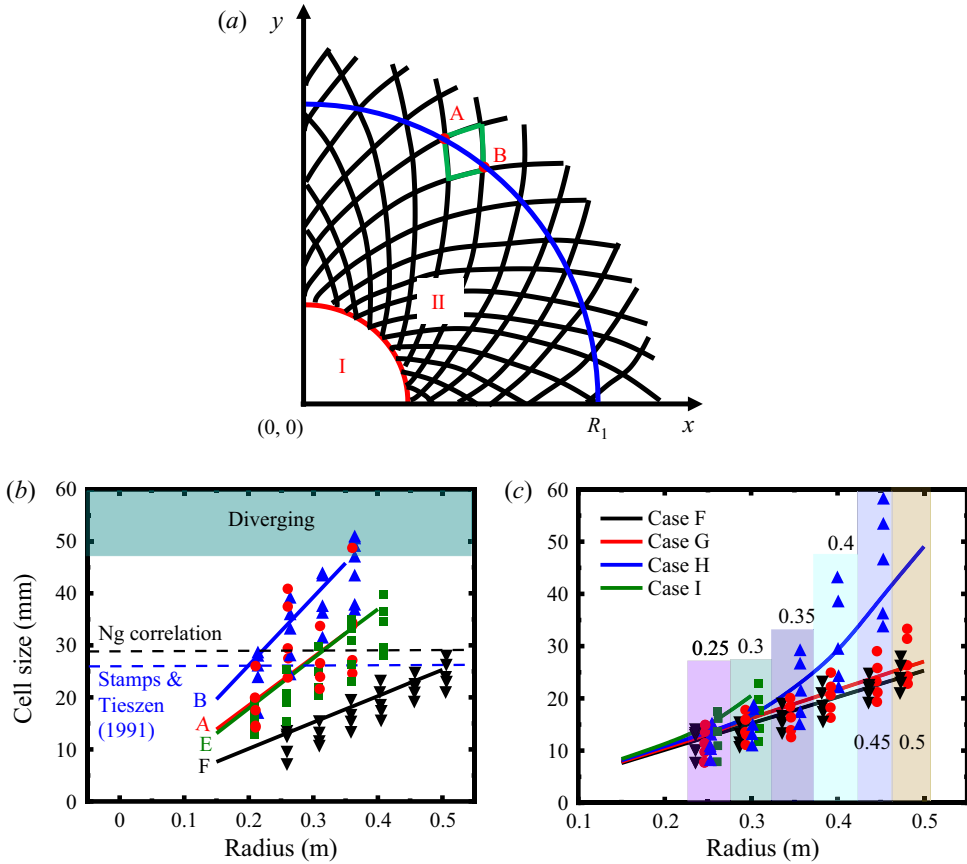
Figure 21. Detonation cell size for different hotspot properties: (*a*) schematic of cell estimation; (*b*) change of detonation cell size along the radial distance in cases A, B, E and F; (*c*) change of detonation cell size along the radial distance in cases F–I. Black dashed line: theoretical data from Ng correlation (Ng *et al.* 2007). Blue dashed line: experimental data with initial pressure of 0.25 atm (Stamps & Tieszen 1991). Number above the histogram: radius of the arc where the cell samples are obtained.

uniform distribution. Furthermore, the maximum cell size is well below the corresponding theoretical and experimental values, and thus it remains at the cell-growth stage even at larger radius, see figure 5(*b*).

In contrast to the uniform mixture cases, only cell coalescence happens in the non-uniform cases. In these cases, the cell size dramatically increases as the ER decreases to match the increased half-reaction length, which makes the detonation more unstable. For better illustration, we put the cell samples horizontally adjacent for different cases at the same radii, as annotated by the columns in figure 21(*c*). Generally, the detonation cell evolutions are similar between cases F ($\varphi = 1$) and G ($\varphi = 1 \rightarrow 0.9$) due to close mixture reactivities. For case H ($\varphi: 1 \rightarrow 0.5$), the cell-growth rate increases considerably across 0.3 m. Meanwhile, the cell sizes become more scattered when $R = 0.3$–0.5 m, due to cell coalescences, see figure 7(*c*). For case I ($\varphi: 1 \rightarrow 0$), the maximum cell size reaches approximately 22 mm at $R = 0.3$ m (corresponding to $\varphi = 0.42$), where the detonation extinction happens.

In addition, the detonation instabilities lead to the irregularity of the detonation cell for a certain mixture composition (Radulescu *et al.* 2005). Here, we quantify the instability
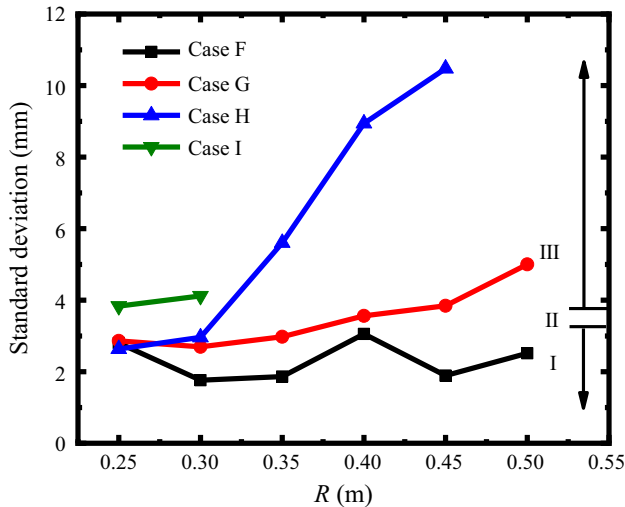
970 A22-22

Figure 22. The SD of the cell size at different radii in cases F−I. Region I: stable; II: weakly unstable; III: unstable.

for a mixture composition by evaluating the detonation cell irregularity (Zhao *et al.* 2016). Since the mixture composition is uniform stoichiometric $H_2 +$ air mixtures in the hotspot property study, we examine the four mixtures with different ER gradients, i.e. $1 \rightarrow 1$ (case F: uniform), $1 \rightarrow 0.9$ (case G: weak decrease), $1 \rightarrow 0.5$ (case H: middle decrease) and $1 \rightarrow 0$ (case I: sharp decrease), which covers all the mixture compositions used in this work.

Figure 22 compares the standard deviation (SD) of the cell size at different radii (thus different ER) in cases F–I. Note that lack of data in case I and H is due to the localized detonation extinction. According to the categorization of mixture stability (Zhao *et al.* 2016), a mixture is considered stable if SD falls in 1.7–3.3 (region I) and unstable if SD exceeds 3.7 (region III), between them, weakly unstable mixtures exist (region II). Generally, the SD in case F (uniform) shows an obviously stable behaviour. Instability increases as the ER decreases, see cases G–I. The mixture remains stable or weakly unstable from ER = 1–0.91 (corresponding to $R = 0.02$–0.45 m in case G). Once the SD approaches the upper limit of weakly unstable state, a sharp rise appears due to a much larger variation of shock-induced ignition delays (Gamezo *et al.* 2000), as shown in cases G ($R = 0.45$–0.5 m) and H ($R = 0.3$–0.45 m), indicating a dramatic increase of the mixture instability.

4.3. *Hydrodynamic structure*

We will further discuss the hydrodynamic thickness variations in expanding cylindrical detonations. The hydrodynamic thickness is the distance between the sonic plane and the SF (Lee & Radulescu 2005). In case B, a self-sustaining diverging detonation is generated. Figure 23 shows the time sequence of shock-frame Mach number in this case. They are from four stages, i.e. overdrive (5–45 μs), cell formation (54–78 μs), growth (100–170 μs) and divergence stages (195–238 μs).

At 5 μs, an overdriven detonation propagates outwardly from the hotspot, and behind it a sub-sonic region exists. This subsonic region is further elongated radially at 20–45 μs, which makes the detonation more susceptible to rarefaction effects from its behind.
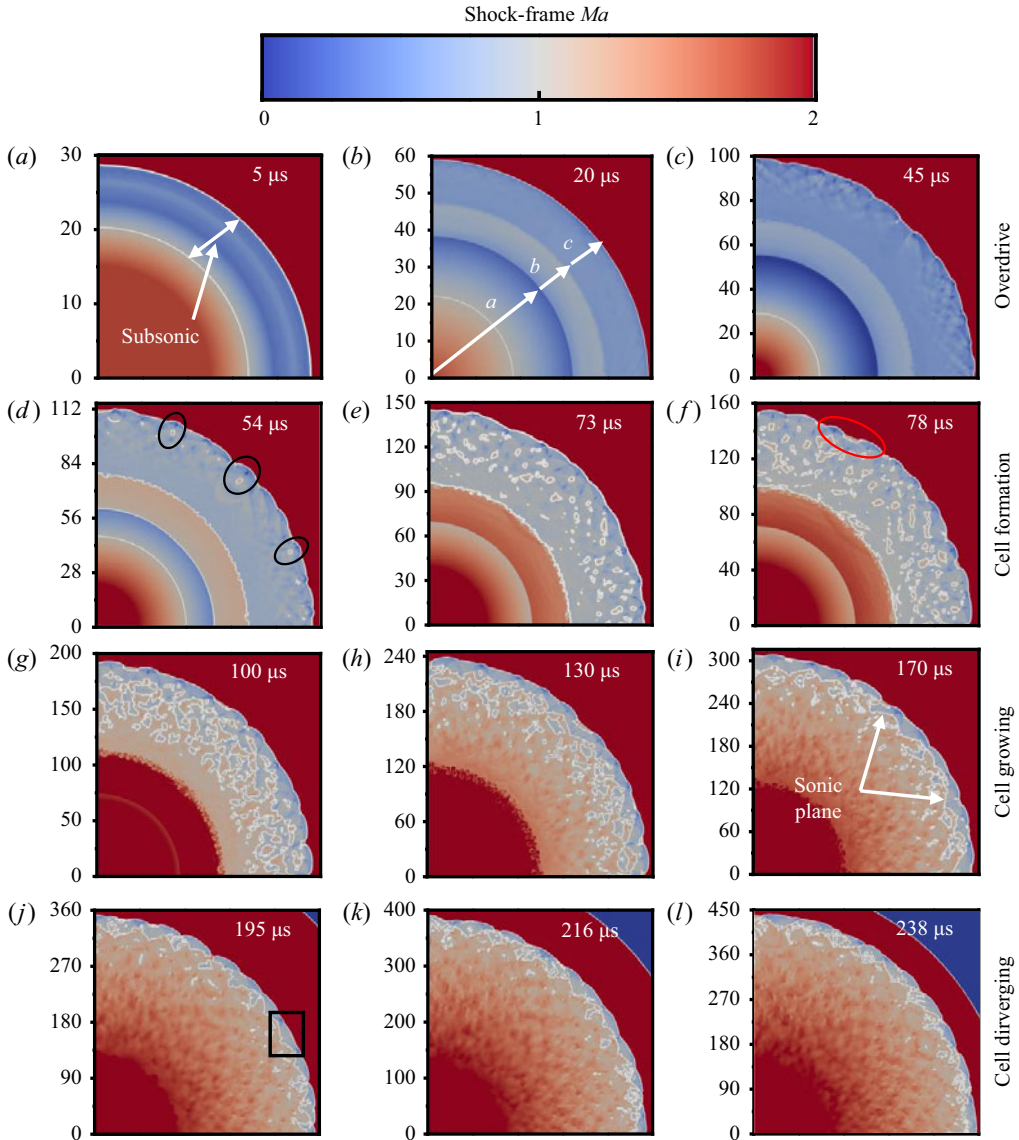
970 A22-23

Figure 23. Changes of shock-frame Mach number in case B. Axis label in millimetres. White line: $Ma = 1$ isolines.

At 20 µs, the flow field behind the detonation is separated into three regions, marked by a, b and c. Specifically, in region a, the dissipation of the hotspot happens, and the gradually reduced Mach number Ma is ascribed to the increasing flow speed. Regions b and c are the burned zones of the deflagration and detonation, respectively. All three regions increase as the detonation expands. Consequently, the transverse disturbance, which is intensified by the curvature, renders the detonation cellularized at 45 µs (Han *et al.* 2017).

At 54 µs, the detonation cellularization becomes more pronounced, accompanied by some scattered supersonic pockets behind the detonation wave. The effect of the expansion waves on the detonation front varies at different circumferential positions. Since the expansion waves cannot penetrate the supersonic pocket to attenuate the detonation (Weber & Olivier 2003), the local detonation fronts ahead of the supersonic pockets
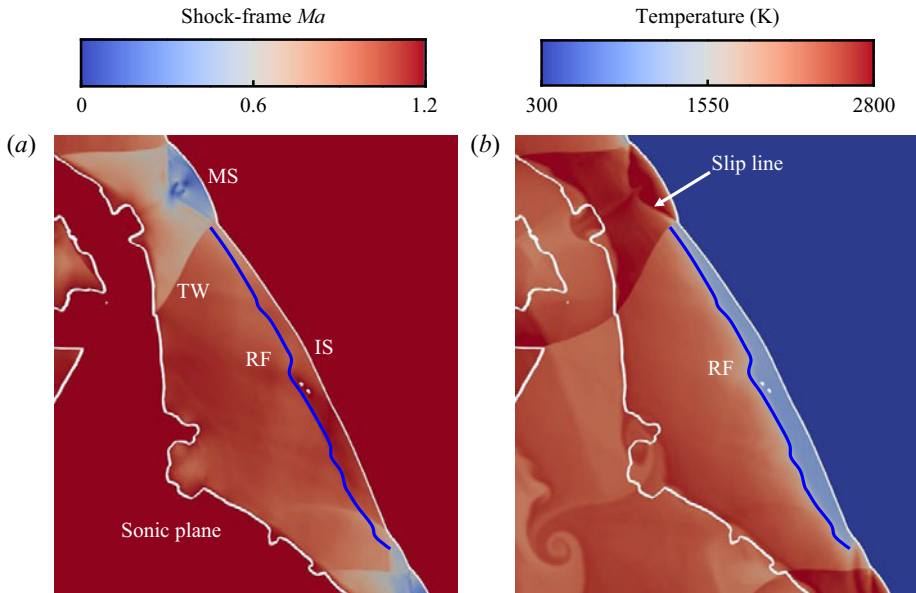
970 A22-24

Figure 24. Contours of (*a*) shock-frame Mach number and (*b*) temperature from the box in figure 23(*j*).
White line: $Ma = 1$. Blue line: RF.

show higher speed, as shown in the circled regions. Meanwhile, there is an increased Mach number behind the leading shock due to the decreased flow speed at 54–78 µs. Especially, a supersonic ring is generated from the subsonic region *b* with two extra sonic lines. At 78 µs, more small supersonic zones are generated behind the detonation front, indicating the enhancement of the hydrodynamic fluctuations. This fluctuation applied to the expansion wave further influences the local detonation intensity, and eventually promotes the formation of the triple-point structure of the detonation front; see the red circles at 78 µs.

At the cell-growth stage (100–170 µs), the localized supersonic pockets gradually coalesce with each other, and are extended to the entire subsonic zone. At 170 µs, a relatively clear sonic region appears immediately behind the SF. Furthermore, the hydrodynamic thickness becomes constant over time, indicating the formation of the freely propagating cylindrical detonation. It is reported in Radulescu *et al.* (2007) that the mechanical and thermal fluctuations decay from a large magnitude (6 %–10 %) close to the SF to a negligible intensity (0.5 %–1 %) at the sonic surface. Therefore, the disturbance behind the sonic plane has little effects on the detonation front, and the detonation evolution is only governed by the available energy release and product expansion between the sonic plane and leading shock (Lee & Radulescu 2005).

At the cell divergence stage (195–238 µs), the subsonic zone only appears between the leading shock and sonic plane as a 'sawtooth' pattern. This is due to the combined effects of transverse wave, IS and MS (Radulescu *et al.* 2007). Figures 24(*a*) and 24(*b*) shows the enlarged Mach number contour (the *Ma* range adjusted to 0–1.2) and the temperature distribution from the box in figure 23(*j*). In the subsonic zone, the Mach number is nearly constant behind the IS, except for the induction zone where the Mach number is higher due to lower temperature, as shown in figure 24(*b*). However, behind the MS, the Mach number increases towards the sonic plane. This is because rapid reactions take place immediately after the MS, which dramatically raises the local temperature and flow speed. A distinct *Ma* discontinuity exists at the interface of post-MS and post-IS products due to the transverse
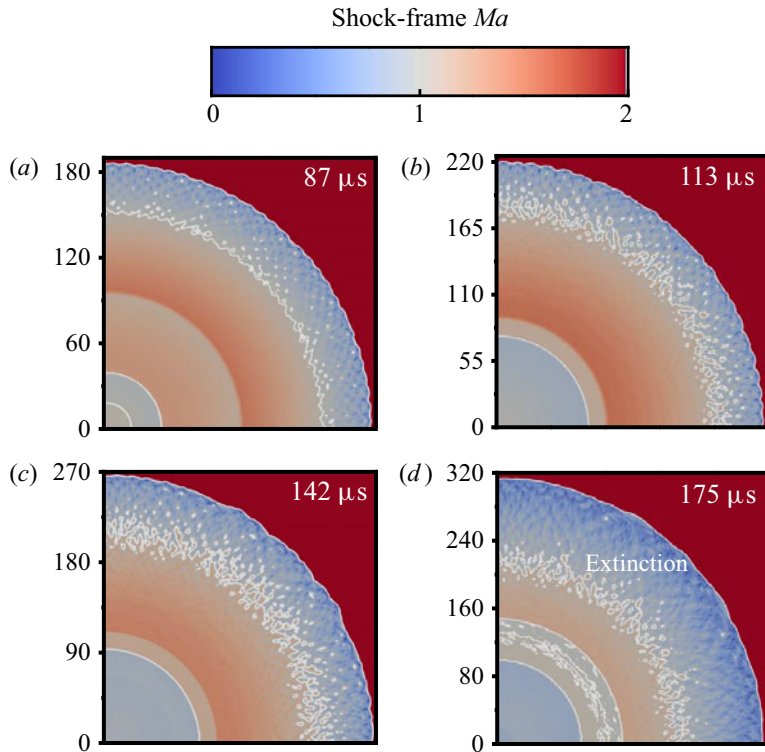
Figure 25. Changes of shock-frame Mach number with time in case I. Axis label in millimetres. White line: $Ma = 1$ isolines.

waves. Owning to the different expansions of post-MS and post-IS products, the sonic plane is convex behind the MS, and concave behind the IS, which leads to the 'sawtooth' pattern of the sonic plane.

Figure 25 shows the time sequence of the Mach number in case I, in which the detonation is ultimately quenched as the equivalence ratio approaches zero. Overall, the shock Mach number gradually decreases when it runs outwardly. At 87 μs, an overdriven detonation with small cells is generated. As a result, the subsonic region behind the leading shock is relatively long (approximately 30 mm). From 113 to 142 μs, plenty of supersonic pockets occur in the subsonic region just like 73–78 μs in figure 23. However, generation and coalescence of the supersonic spot do not make the subsonic region shrink; instead, the subsonic region is further elongated due to the weakened shock intensity at 142 μs. Further downstream the detonation decays to an inert shock with relatively smooth front at 175 μs.

5. Conclusions

Two-dimensional cylindrical detonation direct initiations in hydrogen/air mixtures are computationally studied. The effects of hotspot property and mixture composition gradient on detonation initiation are investigated. The main conclusions are summarized as below.

(i) For non-reactive hotspots, initiation fails for low hotspot pressure ($p_s = 100p_0$ or $150p_0$) and the critical regime dominates for high hotspot pressure ($p_s = 200p_0$ or

970 A22-26

$250p_0$), in which three stages, i.e. no cell, growing cell and diverging cell, occur successively. Supercritical regime dominates for both reactive hotspots ($H_2 + O_2$ or H2 + air, $p_s = 100p_0$). Detonation is directly initiated from the reactive hotspot, whilst it is initiated somewhere beyond the non-reactive hotspot through the coupling of the leading shock and RF.

(ii) The detonation cell size increases almost linearly with the radius at the cell-growth stage, which implies that the cell-family number of the cellular detonation determines the growth rate of cell size in a cylindrical detonation. Furthermore, cell divergence only occurs when the local cell size exceeds the characteristic cell size of a certain value.

(iii) Two cell diverging patterns are identified, i.e. abrupt and gradual patterns. The abrupt divergence is attributed to the generation and intensification of the instability as the cell grows, whilst the gradual divergence is mainly caused by the instability amplification during the interactions between two adjacent shocks. Besides, the cell coalescence occurs if many irregular cells initially form and the cell with smaller cell thickness merges with the bigger one as the detonation expands. As such, the cell-family number is reduced and the local cells grow faster, which leads to an earlier divergence behaviour.

(iv) As the mixture ER decreases linearly from unity at the hotspot vicinity to a certain value at $R = 0.5$ m, the detonation experiences self-sustained propagation, highly unstable propagation (with local extinction) and global extinction with ER: $1 \rightarrow 0.9$, $1 \rightarrow 0.5$ and $1 \rightarrow 0$, respectively. In particular, highly unstable detonation arises from multiple cell coalescences, and detonation extinction occurs where the induction time is highly lengthened and unburned pockets occur.

(v) Hydrodynamic structure analysis is also conducted for both uniform and non-uniform mixtures. For a self-sustaining detonation case (air hotspot, $p_s = 200p_0$), the hydrodynamic thickness first increases at the overdrive stage, then decreases as the detonation cells are generated and eventually reaches almost a constant at the cell divergence stage in which the sonic plane exhibits a 'sawtooth' pattern. This is ascribed to the different expansions of post-MS and post-IS products. For the detonation extinction case ($\varphi: 1 \rightarrow 0$), the hydrodynamic thickness continuously increases from the overdriven state to extinction and no 'sawtooth' sonic plane occurs since no self-sustaining detonation is generated.

Author ORCIDs.
Huangwei Zhang https://orcid.org/0000-0002-5215-5712.

REFERENCES

ASAHARA, M., HAYASHI, A.K., YAMADA, E. & TSUBOI, N. 2012 Generation and dynamics of sub-transverse wave of cylindrical detonation. *Combust. Sci. Technol.* **184**, 1568–1590.

BOECK, L., BERGER, F.J. & SATTELMAYER, T. 2016 Detonation propagation in hydrogen–air mixtures with transverse concentration gradients. *Shock Waves* **26**, 181–192.

BRADLEY, D., MORLEY, C., GU, X.J. & EMERSON, D.R. 2002 Amplified pressure waves during autoignition: relevance to CAI engines. *Tech. Rep.* SAE-2002-01-2868. SAE International.

BURKE, M.P., CHAOS, M., JU, Y., DRYER, F.L. & KLIPPENSTEIN, S.J. 2012 Comprehensive H2/O2 kinetic model for high-pressure combustion. *Intl J. Chem. Kinet.* **44**, 444–474.

CRANE, J., LIPKOWICZ, J.T., SHI, X., WLOKAS, I., KEMPF, A.M. & WANG, H. 2023 Three-dimensional detonation structure and its response to confinement. *Proc. Combust. Inst.* **39** (3), 2915–2923.

DAI, P., CHEN, Z. & GAN, X. 2019 Effects of NOx addition on autoignition and detonation development in DME/air under engine-relevant conditions. *Proc. Combust. Inst.* **37**, 4813–4820.

ECKETT, C.A., QUIRK, J.J. & SHEPHERD, J.E. 2000 The role of unsteadiness in direct initiation of gaseous detonations. *J. Fluid Mech.* **421**, 147–183.

GAMEZO, V.N., VASILIEV, A.A., KHOKHLOV, A.M. & ORAN, E.S. 2000 Fine cellular structures produced by marginal detonations. *Proc. Combust. Inst.* **28** (1), 611–617.

GAO, Y., DAI, P. & CHEN, Z. 2020 Numerical studies on autoignition and detonation development from a hot spot in hydrogen/air mixtures. *Combust. Theor. Model.* **24** (2), 245–261.

GOUSSIS, D.A., HONG, G.I., NAJM, H.N., PAOLUCCI, S. & VALORANI, M. 2021 The origin of CEMA and its relation to CSP. *Combust. Flame* **227** (1), 396–401.

GREENSHIELDS, C.J., WELLER, H.G., GASPARINI, L. & REESE, J.M. 2010 Implementation of semi-discrete, non-staggered central schemes in a colocated, polyhedral, finite volume framework, for high-speed viscous flows. *Intl J. Numer. Meth. Fluids* **63**, 1–21.

GU, X., EMERSON, D. & BRADLEY, D. 2003 Modes of reaction front propagation from hot spots. *Combust. Flame* **133**, 63–74.

GUO, H., XU, Y., LI, S. & ZHANG, H. 2022 On the evolutions of induction zone structure in wedge-stabilized oblique detonation with water mist flows. *Combust. Flame* **241**, 112122.

HAN, W., KONG, W., GAO, Y. & LAW, C.K. 2017 The role of global curvature on the structure and propagation of weakly unstable cylindrical detonations. *J. Fluid Mech.* **813**, 458–481.

HAN, W., KONG, W. & LAW, C.K. 2018 Propagation and failure mechanism of cylindrical detonation in free space. *Combust. Flame* **192**, 295–313.

HAN, W., WANG, C. & LAW, C.K. 2019 Role of transversal concentration gradient in detonation propagation. *J. Fluid Mech.* **865**, 602–649.

HE, L. 1996 Theoretical determination of the critical conditions for the direct initiation of detonations in hydrogen-oxygen mixtures. *Combust. Flame* **104**, 401–418.

HIGGINS, A.J., RADULESCU, M.I. & LEE, J.H. 1998 Initiation of cylindrical detonation by rapid energy deposition along a line. *Symp. Intl Combust.* **27** (2), 2215–2223.

HUANG, Z., CLEARY, M.J. & ZHANG, H. 2020 Application of the sparse-Lagrangian multiple mapping conditioning approach to a model supersonic combustor. *Phys. Fluids* **32**, 105120.

HUANG, Z. & ZHANG, H. 2020 On the interactions between a propagating shock wave and evaporating water droplets. *Phys. Fluids* **32**, 123315.

HUANG, Z., ZHAO, M., XU, Y., LI, G. & ZHANG, H. 2021 Eulerian-Lagrangian modelling of detonative combustion in two-phase gas-droplet mixtures with OpenFOAM: Validations and verifications. *Fuel* **286**, 119402.

JIANG, Z., HAN, G., WANG, C. & ZHANG, F. 2009 Self-organized generation of transverse waves in diverging cylindrical detonations. *Combust. Flame* **156**, 1653–1661.

JIN, S., XU, C., ZHENG, H. & ZHANG, H. 2023 Detailed chemistry modelling of rotating detonations with dilute n-heptane sprays and preheated air. *Proc. Combust. Inst.* **39** (4), 4761–4769.

KASIMOV, A.R. & STEWART, D.S. 2004 Theory of direct initiation of gaseous detonations and comparison with experiment. *Tech. Rep.* 1043. University of Illinois Urbana-Champaign.

KURGANOV, A., NOELLE, S. & PETROVA, G. 2001 Semidiscrete central-upwind schemes for hyperbolic conservation laws and Hamilton–Jacobi equations. *SIAM J. Sci. Comput.* **23** (3), 707–740.

LEE, J.H. 1984 Dynamic parameters of gaseous detonations. *Annu. Rev. Fluid Mech.* **16**, 311–336.

LEE, J.H. 2008 *The Detonation Phenomenon*. Cambridge University Press.

LEE, J.H., KNYSTAUTAS, R. & GUIRAO, C. 1982 The link between cell size, critical tube diameter, initiation energy and detonability limits. *Proceedings of the International Conference on Fuel-Air Explosions*, pp. 157–187. University of Waterloo Press.

LEE, J.H. & RADULESCU, M. 2005 On the hydrodynamic thickness of cellular detonations. *Combust. Explos. Shock Waves* **41**, 745–765.

LEE, J.H. & RAMAMURTHI, K. 1976 On the concept of the critical size of a detonation kernel. *Combust. Flame* **27**, 331–340.

LU, X., KAPLAN, C.R. & ORAN, E.S. 2023 Transition to detonation in inhomogeneous hydrogen-air mixtures: the importance of gradients in detonation cell size. *Proc. Combust. Inst.* **39** (3), 2777–2785.

LU, T., YOO, C.S., CHEN, J. & LAW, C.K. 2010 Three-dimensional direct numerical simulation of a turbulent lifted hydrogen jet flame in heated coflow: a chemical explosive mode analysis. *J. Fluid Mech.* **652**, 45–64.

MATSUI, H. & LEE, J. 1976 Influence of electrode geometry and spacing on the critical energy for direct initiation of spherical gaseous detonations. *Combust. Flame* **27**, 217–220.

MAZAHERI, K. 1997 Mechanism of the onset of detonation in blast initiation. PhD thesis, McGill University, Montreal, Canada.

NG, H.D. 2005 The effect of chemical reaction kinetics on the structure of gaseous detonations. PhD thesis, McGill University, Montreal, Canada.

NG, H.D., JU, Y. & LEE, J.H. 2007 Assessment of detonation hazards in high-pressure hydrogen storage from chemical sensitivity analysis. *Intl J. Hydrogen Energy* **32**, 93–99.

NG, H.D. & LEE, J.H. 2003 Direct initiation of detonation with a multi-step reaction scheme. *J. Fluid Mech.* **476**, 179–211.

PINTGEN, F., ECKETT, C., AUSTIN, J. & SHEPHERD, J. 2003 Direct observations of reaction zone structure in propagating detonations. *Combust. Flame* **133**, 211–229.

QI, C. & CHEN, Z. 2017 Effects of temperature perturbation on direct detonation initiation. *Proc. Combust. Inst.* **36** (2), 2743–2751.

RADULESCU, M., HIGGINS, A., MURRAY, S. & LEE, J. 2003 An experimental investigation of the direct initiation of cylindrical detonations. *J. Fluid Mech.* **480**, 1–24.

RADULESCU, M.I., SHARPE, G.J., LAW, C.K. & LEE, J.H. 2007 The hydrodynamic structure of unstable cellular detonations. *J. Fluid Mech.* **580**, 31–81.

RADULESCU, M.I., SHARPE, G.J., LEE, J.H.S., KIYANDA, C.B., HIGGINS, A.J. & HANSON, R.K. 2005 The ignition mechanism in irregular structure gaseous detonations. *Proc. Combust. Inst.* **30**, 1859–1867.

REGELE, J.D., KASSOY, D.R., ASLANI, M. & VASILYEV, O.V. 2016 Evolution of detonation formation initiated by a spatially disturbuted, transient energy source. *J. Fluid Mech.* **802**, 305–332.

SHEN, H. & PARSANI, M. 2017 The role of multidimensional instabilities in direct initiation of gaseous detonations in free space. *J. Fluid Mech.* **813**, 1–13.

SHEN, H. & PARSANI, M. 2019 Large-scale computation of direct initiation of cylindrical detonations. In *31st International Symposium on Shock Waves*, pp. 61–67. Springer.

SHEPHERD, J.S. AND DETONATION TOOLBOX. 2021 Version. Available at: https://shepherd.Caltech.Edu/edl/publicresources/sdt/.

SHORT, M. & STEWART, D.S. 1999 The multi-dimensional stability of weak-heat-release detonations. *J. Fluid Mech.* **382**, 109–135.

SOURY, H. & MAZAHERI, K. 2009 Utilizing unsteady curved detonation analysis and detailed kinetics to study the direct initiation of detonation in H_2–O_2 and H_2–Air mixtures. *Intl J. Hydrogen Energy* **34** (24), 9847–9856.

STAMPS, D.W. & TIESZEN, S.R. 1991 The influence of initial pressure and temperature on hydrogen-air-diluent detonations. *Combust. Flame* **83**, 353–364.

SU, J., DAI, P. & CHEN, Z. 2021 Detonation development from a hot spot in methane/air mixtures: effects of kinetic models. *Intl J. Engine Res.* **22** (8), 2597–2606.

SUN, J., TIAN, B. & CHEN, Z. 2023 Effect of ozone addition and ozonolysis reaction on the detonation properties of C_2H_4/O_2/Ar mixtures. *Proc. Combust. Inst.* **39** (3), 2797–2806.

WATT, S.D. & SHARPE, G.J. 2004 One-dimensional linear stability of curved detonations. *Proc. R. Soc. Lond.* A*: Math. Phys. Engng Sci.* **460**, 2551–2568.

WATT, S.D. & SHARPE, G.J. 2005 Linear and nonlinear dynamics of cylindrically and spherically expanding detonation waves. *J. Fluid Mech.* **522**, 329–356.

WEBER, M. & OLIVIER, H. 2003 The thickness of detonation waves visualised by slight obstacles. *Shock Waves* **13**, 351–365.

WOLANSKI, P. 2013 Detonative propulsion. *Proc. Combust. Inst.* **34** (1), 125–158.

XU, Y., ZHAO, M. & ZHANG, H. 2021 Extinction of incident hydrogen/air detonation in fine water sprays. *Phys. Fluids* **33**, 116109.

ZELDOVICH, I.B. 1956 An experimental investigation of spherical detonation of gases. *Sov. Phys. Tech. Phys.* **1**, 1689–1713.

ZHANG, B. & BAI, C. 2014 Methods to predict the critical energy of direct detonation initiation in gaseous hydrocarbon fuels–an overview. *Fuel* **117**, 294–308.

ZHANG, B., NG, H.D. & LEE, J.H. 2012 The critical tube diameter and critical energy for direct initiation of detonation in C2H2/N2O/Ar mixtures. *Combust. Flame* **159**, 2944–2953.

ZHAO, M., CLEARY, M.J. & ZHANG, H. 2021 Combustion mode and wave multiplicity in rotating detonative combustion with separate reactant injection. *Combust. Flame* **225**, 291–304.

ZHAO, H., LEE, J.H., LEE, J. & ZHANG, Y. 2016 Quantitative comparison of cellular patterns of stable and unstable mixtures. *Shock Waves* **26**, 621–633.